The effects of laser polarization and wavelength on injection dynamics of a laser wakefield accelerator

Y. Ma[1,a)] D. Seipt[1,4,5], A. E. Hussein[1,6], S. Hakimi[2], N. F. Beier[2], S. B. Hansen[3], J. Hinojosa[1], A. Maksimchuk[1], J. Nees[1], K. Krushelnick[1], A. G. R. Thomas[1], and F. Dollar[2]

[1]*Gérard Mourou Center for Ultrafast Optical Science, University of Michigan, Ann Arbor, Michigan 48109, USA*

[2]*Department of Physics and Astronomy, University of California, Irvine, California 92697, USA*

[3]*Sandia National Laboratories, Albuquerque, New Mexico 87185, USA*

[4]*Helmholtz Institut Jena, Fröbelstieg 3, 07743 Jena, Germany*

[5]*GSI Helmholtzzentrum für Schwerionenforschung GmbH, Planckstrasse 1, 64291 Darmstadt, Germany and*

[6]*Department of Electrical and Computer Engineering, University of Alberta, Edmonton, Alberta T6G 1H9 Canada*

Here, we investigate the effects of laser polarization and wavelength on electron injection dynamics in a laser wakefield accelerator. During the ionization process, electrons gain residual momentum and kinetic energy via above threshold ionization, which has a strong dependence on laser polarization. A circularly polarized laser pulse results in a much higher residual momentum and kinetic energy gain for the ionized electrons compared with the linearly polarized case. This residual momentum results in particle injection because of the sensitivity of particle trapping to the initial conditions and enhanced the total injected beam charge in both experiments and particle-in-cell simulations. Due to the strong correlation of above threshold ionization with laser wavelength, in this work we extended the investigation to long wavelength (up to 20 μm) drive pulses using particle-in-cell simulations. Owing to the gain in kinetic energy, it may be expected that the charge trapped would consistently increase for circular polarization with increasing laser wavelength, but this was not observed. Instead there are oscillations with wavelength in the relative trapped charge between linear and circular polarization cases, which arise because of ionization and heating effects on the plasma. Our studies highlight the complex interplay between several different physical effects, including injection regimes — above threshold ionization assisted injection, wave-breaking injection by carrier-envelope-phase effects and ionization injection — ionization gradient induced self-compression and thermal modifications to the wake structure that need considering when extrapolating laser wakefield acceleration to different wavelength regimes.

I. INTRODUCTION

Laser wakefield acceleration (LWFA)[1] is a promising alternative to large scale radio-frequency accelerators due to its ultra-high accelerating gradients (~100 GeV/m)[2]. The past two decades have witnessed many important milestones for LWFA, including the famous "dream beam" work reporting the first generation of quasi-monoenergetic electron beams[3–5], and the generation of multi-GeV electron beams[6–9]. However, there are still several aspects limiting its practical application to be addressed[10]. For example, it is difficult to further increase beam energy beyond GeV, especially for the goal of driving future colliders for high energy physics. To push the electron energy up to TeV level, many schemes have been conceived, such as the staging concept based on multiple laser wakefield accelerators[11], and recently single-stage dephasingless LWFA based on spatial-temporal control of the laser pulse has also been proposed[12–14].

Another limitation is the repetition rate of LWFA, mainly restricted by the repetition-rate of laser driver technologies and the plasma target. Most experiments are performed with ~ 1 μm lasers to date, but to achieve the high repetition-rates required for applications, other wavelength technologies may be required, and so it is important to fully understand the implications of wavelength on the plasma accelerator performance. Recently, a significant progress has been made which reported stable generation of hundreds of MeV electron beams over 100,000 continuous shots at 1 Hz[15], demonstrating the robustness of LWFA as well as making it more appealing. Moreover, many applications, such as seeding table-top X-ray free electron laser[16,17] and strong-field quantum electrodynamics experiments[18,19], require extremely high electron beam quality in terms of energy spread, emittance, dark current, etc. The electron beam quality has a strong correlation with the dynamics of the electron injection into the bubble and the subsequent acceleration process. Thus, understanding and controlling of the injection dynamics are crucial for advancing the development of LWFA.

Because of the rapid development of ultra-intense femtosecond laser systems[20], LWFA is typically performed in the nonlinear "bubble" regime[21,22] owing to the desirable linear longitudinal accelerating and transverse focusing

[a)]Electronic mail: yongm@umich.edu

fields. In an underdense plasma, the laser ponderomotive force pushes background plasma electrons sideways, producing a bubble-like plasma wave. Electrons with sufficient longitudinal velocity could be trapped by the plasma wave, resulting in so-called self-injection. The wakefield is driven by the ponderomotive force, which depends on the gradient of the laser intensity envelope and thus has no dependence on laser polarization. Therefore, it has been believed that the self-injection in LWFA is polarization-independent with the evidence of the isotropic electron beam profile and the associated betatron X-ray beam profile[23,24]. However, at the very early stage of a nonlinear LWFA with neutral gas target, the laser pulse front ionizes the gas medium to generate the ambient plasma. Thus, ionization is involved. It is clear that ionization is polarization-dependent due to the well-known above threshold ionization[25] (ATI) process. In this process, electrons absorb more photons than needed to be released from the atom, resulting in a residual kinetic momentum and kinetic energy gain. The transverse momentum gain can be expressed as $\mathbf{p}_\perp = m_e c\mathbf{a}_i$, where $\mathbf{a}_i = e\mathbf{A}_i/m_e c$ is the normalized laser vector potential when electrons were ionized. The longitudinal momentum varies as $p_\parallel = m_e c\mathbf{a}_i^2/2$, and the kinetic energy gain as $E_{kin} \simeq p_\parallel c$[26–28]. The longitudinal momentum and the kinetic energy gain depend on the laser polarization as:

$$p_\parallel = \frac{m_e c a_i^2}{2}\begin{cases}\sin^2\phi_0, & \text{for LP}\\ 1, & \text{for CP}\end{cases} \tag{1}$$

where ϕ_0 is the laser phase, LP stands for linear polarization and CP stands for circular polarization. The residual momentum and energy of the electrons in the LP case should vanish since electrons will always be released at the crest of the electric field under the strong-field ionization regime where $a_i = 0$ due to the fact that the vector potential is always $\pi/2$ out of phase with the electric field. While in the CP case, the vector potential never vanishes but only rotates, thus always giving rise to momentum and kinetic energy gain. Moreover, the ATI process has a strong dependence on the laser wavelength as $a_i \propto \lambda_L$. Therefore, for the same laser intensity, the kinetic energy gain of the ionized electrons, and hence the plasma temperature (defined as the average kinetic energy per particle) can be enhanced with long-wavelength laser pulses. It has previously been shown that an underlying thermal plasma distribution can significantly affect particle trapping and the maximum wave amplitude in plasma accelerators[29–38]. It is therefore expected that the ATI effect should start modifying the plasma wake structure and trapping conditions as the temperature increases. Moreover, it has previously been shown that ionization gradients can lead to self-compression of the laser pulse[39,40], which will also modify trapping conditions. The interplay between all of these processes is important to understanding the behavior of LWFA with different wavelength driver pulses.

In this paper, we will examine how the polarization-dependent ATI process and the laser wavelength affect the dynamics of electron injection and wakefield formation in LWFA through both experiments and numerical simulations. The paper summarizes the work already published in ref.[41], with additional data not published in that paper, and then extends the study through extensive particle-in-cell simulations to a broad range of laser wavelengths. This paper is organized as follows. In Sec. II, the laser polarization and wavelength effects of the ATI process on the momentum and energy gain of the ionized electrons, as well as on the plasma temperature, will be illustrated. Sec. III will give the comparison of electron injection in LWFA with LP and CP lasers for both experimental measurements and numerical simulations. In Sec. IV, we will demonstrate the interplay between different injection mechanisms due to laser polarization and wavelength effects. The conclusion will be given in Sec. V.

II. ABOVE THRESHOLD IONIZATION WITH HELIUM TARGETS

To illustrate the polarization effects on the particle momentum distribution after ionization, we performed 1D3V particle-in-cell (PIC) simulations by using the code EPOCH[42] with the Ammosov-Delone-Krainov (ADK) ionization model[43]. The gas medium was neutral helium.

The ionization potential for the two helium electrons are: $e1$ ($He^0 \rightarrow He^+$) 24.59 eV and $e2$ ($He^+ \rightarrow He^{2+}$) 54.42 eV, respectively. The ionization appearance intensity is $I_{\rm app}[\mathrm{W/cm^2}] = 8\times10^9\, E^4_{\rm ion}[\mathrm{eV}]/Z^2 = 7.3\times10^{14}$ $[1.8\times10^{16}]$ for $e1$ $[e2]$ according to the barrier suppression ionization (BSI) model[44]. This corresponds to a vector potential of $a_i(e1) \simeq 0.013$ and $a_i(e2) \simeq 0.064$ for a CP laser with a wavelength of 800 nm, which gives a kinetic energy of $E_{kin}(e1) \simeq 0.2$ keV and $E_{kin}(e2) \simeq 1.1$ keV.

Figure 1 shows the obvious difference on the ionization process due to the laser polarization state. As we can see from the ionized electron density front for an LP laser in Fig. 1(b), there are several discrete steps for both helium electrons. The small regions between two neighboring steps are where the electrons were released. These correspond to the phase where the laser electric field is at the maximum in each half-cycle, as shown in Fig 1(a). In this case, the electric field crests are where the vector potential $a_i = 0$. Thus electrons gain no momentum and energy according to Eq. (1). On the contrary, the electron density fronts in the CP laser case are continuous, as shown in Fig. 1(d), due to the continuous overall electric field in Fig. 1(c). Electrons will always gain momentum and energy since the vector potential will be non-zero when they were released. The comparisons of the residual transverse momentum and kinetic energy gain after the electrons left the laser field are given in Fig. 1(e)[41]. One can see a clear spiral pattern for the momentum

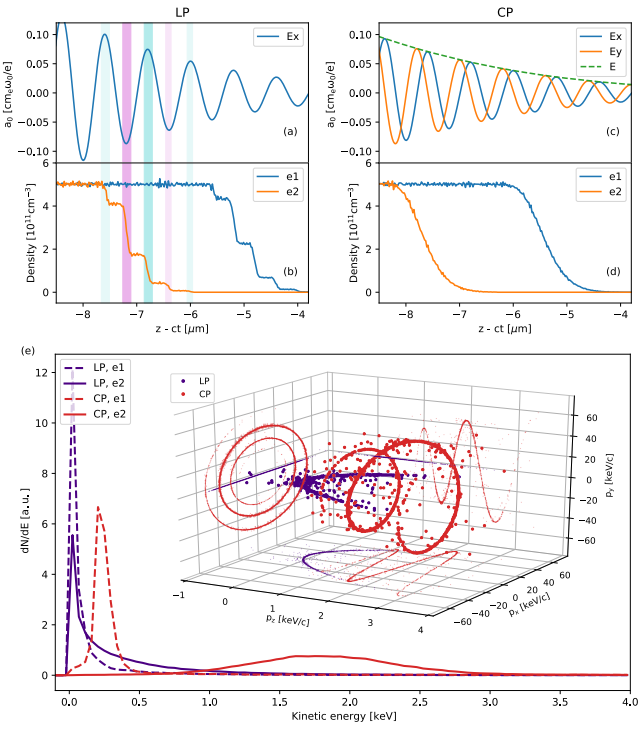

FIG. 1. Polarization-dependent ionization 1D PIC simulations. (a) and (b) show the laser pulse front and ionized electron density fronts for the LP case. (c) and (d) show the laser pulse front and ionized electron density fronts for the CP case. (e) gives the kinetic energy gain of the two electrons in both LP and CP cases. The inset of (e) shows the corresponding phase space of transverse and longitudinal momenta. In these simulations, the laser pulses have a wavelength of 800 nm, a peak intensity of 1×10^{18} W/cm^2, the plasma densities are as low as 1×10^6 cm^{-3} to minimize collective effects in the plasma.

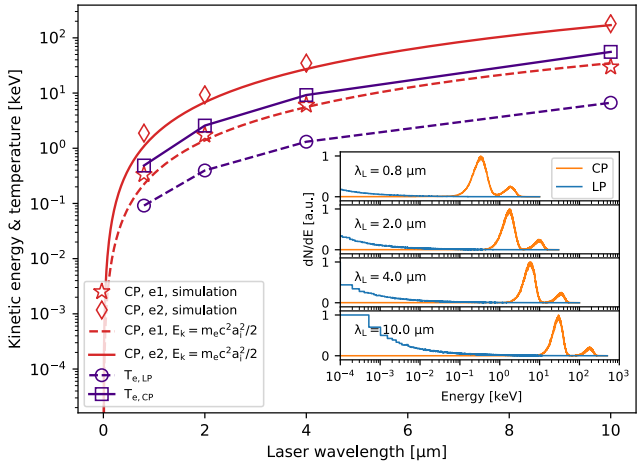

FIG. 2. Wavelength effects on kinetic energy gain and plasma temperature. The red solid and dashed lines represent the theoretical predictions of the kinetic energy gain for the two helium electrons, while the red diamonds and stars are from simulations. The purple solid and dashed line show the plasma temperature for CP and LP cases, respectively. The inset figures show the energy distributions of the ionized electrons with four different wavelengths for both CP and LP cases. All the simulation parameters, except for the laser wavelength, are the same as those in Fig. 1.

phase space distributions (p_x, p_y, p_z) for the CP case and a resulting kinetic energy gain on the order of keVs, which agrees with the BSI estimation. One should note that, the transverse momentum and kinetic energy gain for the LP case is not completely zero, due to a phase mismatch on the laser field front[25] (Fig. 1(a)) which can be confirmed by the finite width steps on the density front (Fig. 1(b)).

As we have discussed above, the laser wavelength has a strong influence on the ATI process hence the kinetic energy gain of the ionized electrons as well as the plasma temperature. This was also confirmed by 1D PIC simulations, as shown in Fig. 2. We examined the peak kinetic energies for the two helium electrons for the CP case with wavelengths of 0.8, 2.0, 4.0 and 10 μm, which agree well with the theoretical predictions. We also compared the overall plasma temperature contributed by both electrons between CP and LP cases. For all wavelengths, the plasma temperature for CP case is always approximately an order of magnitude higher than that in the LP case. Meanwhile, the longer the laser wavelength, the higher the resulting kinetic energy and plasma temperature. It is worth noting that the plasma temperature for a CP 10 μm laser, for example, is on the order of 100 keV. This temperature is remarkably high, approaching the rest mass energy of the electrons, and results in significant thermal modifications to the bulk plasma dynamics.

III. POLARIZATION EFFECTS ON SELF-INJECTION WITH 800 NM LASERS

The polarization effects of the ATI process on the momentum and energy gain of the ionized electrons is clearly illustrated in Sec. II. In this section, we would like to investigate whether such effects would play a role in LWFA with the most prevailing laser wavelength of 800 nm.

A series of PIC simulations were performed to examine the polarization effects on both the plasma physics and the ionization physics during LWFA with CP and LP drive lasers, using the quasi-3D code FBPIC[45]. Detailed simulations parameters can be found in Ref.[41].

The polarization effects on plasma dynamics were illustrated in Fig. 3, where Fig. 3(a) compares the wake potentials between the CP (top half) and LP (bottom half) cases, Fig. 3(b) compares the laser pulse intensity evolution between the two cases with a series of different plasma densities. As mentioned above, the wakefield is driven by the polarization-independent ponderomotive force and for 800 nm the induced plasma temperature is still relatively low. So we would expect the same wake-

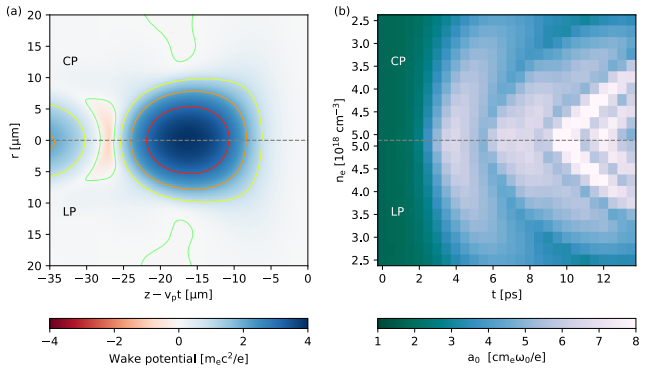

FIG. 3. (a) Comparison of the wake potential between CP (upper) and LP (lower) cases. The simulation parameters are: $\lambda_L = 800$ nm, $a_0^{LP} = \sqrt{2}\ a_0^{CP} = 1.6$, $w_0 = 26\ \mu$m, He gas density $n_{\rm He} = 2.0 \times 10^{18}{\rm cm}^{-3}$. (b) Comparison of the peak laser intensity evolution between CP (upper) and LP (lower) cases for a series of plasma densities. Other parameters are the same as in (a).

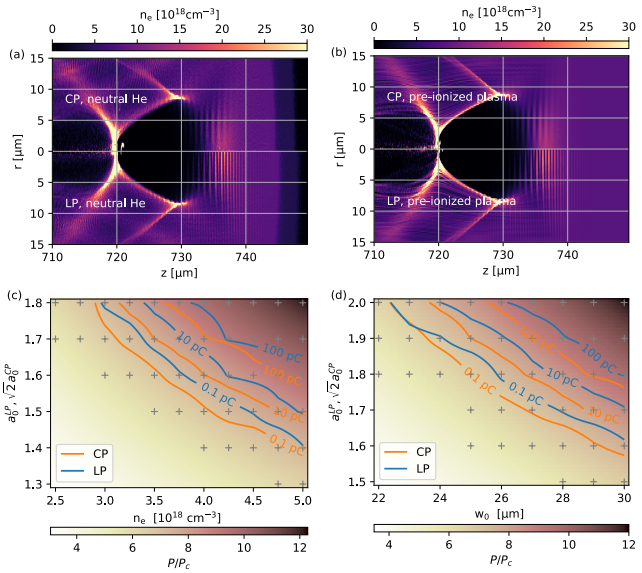

FIG. 4. Comparison of plasma density distribution with (a) neutral He gas and (b) pre-ionized plasma between CP (upper) and LP (lower) cases. The simulation parameters are the same as those in Fig. 3(a) for the neutral He case, while in the pre-ionized plasma case, the plasma density is $n_e = 2n_{\rm He} = 4 \times 10^{18}{\rm cm}^{-3}$. (c) and (d) show the injected electron beam charge in parameter spaces of (a_0, n_e) and (a_0, w_0), respectively. In (c), the laser spot size was fixed as $w_0 = 26\ \mu$m, while in (d), the helium density was fixed at $n_{\rm He} = 1.5 \times 10^{18}$ cm^{-3}. Each gray cross represents two different simulations runs with either CP or LP lasers and otherwise the same parameters.

field structures, which can be confirmed by Fig. 3(a), in which the wake potentials for CP and LP cases are almost identical. This indicates the plasma response to the laser pulses are the same. On the other hand, the evolution of the laser pulse intensity demonstrates the response of the laser pulse to the plasma. As we can see from Fig. 3(b), in a wide plasma density range, the difference of laser intensity evolution between CP and LP cases is only about 0.4%. Therefore, the laser polarization shows no significant impact on plasma dynamics in LWFA.

However, for the same simulations, we observed different self-injection phenomena, as shown in Fig. 4(a), in which we can see obvious electron injection with a CP laser while almost no injection is observed with an LP laser. Furthermore, we studied the difference between CP and LP cases with pre-ionized plasma, as shown in Fig. 4(b). With pre-ionized plasma, the laser polarization doesn't affect the bubble structure and the injection significantly. Moreover, the fact that there is no significant difference between the cases of neutral helium and pre-ionized plasma in LP case indicates that ionization physics itself plays no significant role in injection in the case of low-Z material targets. This is different from the well-known ionization injection regime[46–48] with mid-Z materials such as nitrogen and oxygen in which case the ionization happens inside the plasma bubble. Therefore, it is the polarization-dependent ionization that dominates the injection seen in the case of a CP laser with neutral helium targets.

To better understand the injection dynamics, we examined the initial position of the injected electrons in the co-moving frame. It turns out that in the CP case the trapped electrons originate from a spiral structure at the evolving ionization front and the projection in the transverse plane is a ring with a width of approximately 1 μm and a diameter close to the laser spot size. In contrast, the trapped electrons in the LP case originate from the vicinity of only two particular angles in the polarization plane[41]. The spiral structure in the CP case occurs because the transverse vector potential at ionization induces an asymmetry to the electron orbits that follow the bubble sheath. At a certain time, the initial positions of the trapped electrons are all located within a small azimuthal angle where the vector potential points toward the axial axis. As the vector potential rotates, a spiral structure forms. In fact, the two-angle feature in the LP case indicates that the injection mechanism is fundamentally different from the typical self-injection regime, in which electrons are pushed by the ponderomotive force and originate from any angle which eventually results in an isotropic distribution. Moreover, approximately 100% of the injected electrons come from $e2$ for the CP case, while only about 75% for the LP case. Thus, the scenario of electron injection with a CP laser is completely different from the case of an LP laser.

The role of the polarization-dependent ionization can be even better illustrated in more broad parameter spaces. We explored the the difference of the injected beam charge and the injection threshold between CP and LP cases with neutral helium in parameter spaces

of (a_0, n_e) and (a_0, w_0), as shown in Fig. 4(c)[41] and (d), respectively. Both of these two 2D parameter spaces correspond to a 1D space of the ratio of laser power over critical power for self-guiding as $P/P_c \propto a_0^2 w_0^2 n_e$, where $P_c[\mathrm{GW}] = 17.4\ (n_c/n_e)$.[49] For almost all the simulation runs, we observed a higher beam charge in the CP case. Besides, the required laser power for the same beam charge was lowered for the CP case. This demonstrated that the injection threshold can be lowered by using CP lasers. It also indicates a new injection mechanism due to the polarization-dependent ATI process. We shall refer it to "ATI injection" from now on.

The simulation results were further confirmed by experiments performed at the HERCULES laser facility at the Gérard Mourou Center for Ultrafast Optical Science at the University of Michigan[41]. To switch the laser polarization between LP and CP, a quarter-wave plate made of mica with a thickness 40 μm was placed into the beam path before an f/20 off-axis parabolic mirror. The polarization can be easily switched without changing the laser intensity and focus quality by rotating the wave plate by 45 degrees. The target was pure helium filled in a 3D-printed gas cell[50] to avoid potential self-injection caused by plasma density ripples[51].

Figure. 5(a)[41] shows the comparison of injected beam charge as a function of plasma density between CP and LP cases with the same laser power of $P = 50.4 \pm 5.4$ TW. The density threshold for injection in CP and LP cases are $2.7 \times 10^{18}\mathrm{cm}^{-3}$ and $3.2 \times 10^{18}\mathrm{cm}^{-3}$, respectively. This corresponds to a lowered threshold ratio of $P/P_c = 4.6$ for the CP case from $P/P_c = 5.5$ for the LP case. Figures 5(b) shows the total electron beam charge with two different laser power at 50.4 ± 5.4 TW and 68.3 ± 6.1 TW. In both cases, CP results in a higher beam charge. For the low power case, the beam charges with LP and CP lasers are 1.5 ± 0.7 pC and 8.6 ± 2.3 pC, respectively. In the high power case, the beam charges are 10.9 ± 3.0 pC and 50.0 ± 5.9 pC for LP and CP, respectively. The inset figures highlight the comparison of electron beam reproducibilities with CP and LP at the same plasma density of $n_e = (3.8 \pm 0.4) \times 10^{18}$ cm^{-3} for the two laser power cases. The reproducibility improvement with CP is obvious for both laser powers. It should be noted that, in addition to the laser power and polarization, the data set (IV) has a different gas cell to that used for data sets (I-III). Although the measured plasma density was nominally the same, it is possible that the differences between the gas cells also contributed to the differences between data sets (III) and (IV). The direct comparison between data sets (I) and (II) published in our paper[41] used the same gas cell with data taken on the same day, switching between polarizations to ensure a well controlled test. This additional data comparison of data sets (III) and (IV), while not as well controlled, nevertheless is consistent with the conclusions supported by data sets (I) and (II).

Moreover, the different transverse momentum and kinetic energy gain due to different laser polarization will result in different plasma temperatures[52,53], which can be determined from the time-integrated XUV photon emission. With the electron spectra in Fig. 1(g), we simulated the XUV spectra with the atomic physics code SCRAM[54]. The atomic simulation results show that CP always results in more photon emission[41]. This was also confirmed by the experimental measurement with a flat-field XUV spectrometer[55] with various gas pressures[41]. It is worth noting that, although a CP laser leads to a higher plasma temperature, it is not the main reason for the injection in CP case with 800 nm lasers. Plasma temperature effects will be discussed in detail in Sec. IV.

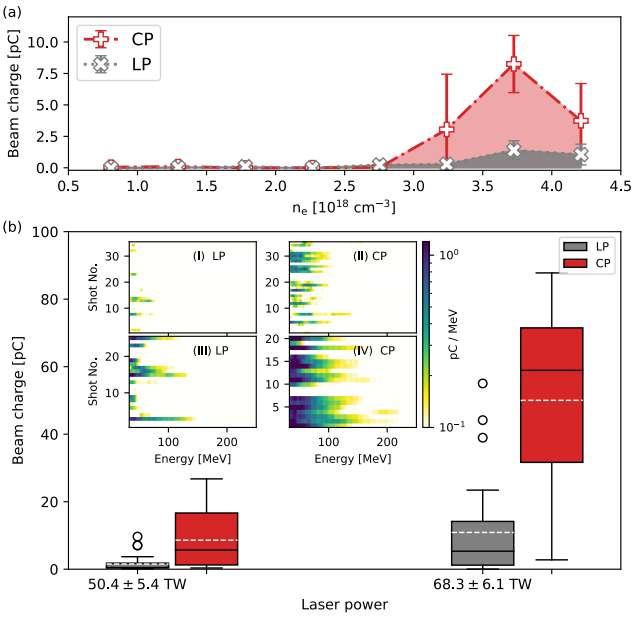

FIG. 5. (a) Injected electron beam charge as a function of plasma density with fixed laser power. (b) Total electron beam charge at two different values of laser power for both LP and CP cases. In the box-plot, white dashed lines represent the mean measured charges, while black lines represent the medians, and 50% of the data are inside the boxes. The inset figures show the electron spectra of a series of consecutive shots with low laser power (I and II) and high laser power (III and IV) for LP and CP cases, respectively, with fixed plasma density. Note that, except for the laser power and polarization, I, II and III have identical conditions, while IV was performed with a new gas cell but with the same measured plasma density.

IV. LASER WAVELENGTH EFFECTS ON THE INTERPLAY OF INJECTION MECHANISMS

In Sec. III, we have demonstrated the role of the polarization-dependent ATI process on electron self-injection. Because of the phase-dependent ionization process and the higher momenta and kinetic energy gain, a CP laser can lead to a different self-injection mechanism due to the non-vanishing vector potential and reduce the

injection threshold. The ATI process also has a strong dependence on laser wavelength, as illustrated in Fig. 2. As the laser wavelength increases, the kinetic energy of ionized electrons as well as the plasma temperature increases non-linearly. We would expect a more dominant "ATI injection" in the long wavelength regime. Thus, we scaled the PIC simulations in Fig. 4 to long wavelength laser drivers (up to 20 μm).

The basic principles to scale LWFA to long wavelength are as follows:

1. Maintain the ratio of the plasma density to critical density as a constant, $n_e/n_c = const.$
2. Maintain the pulse duration over the plasma wavelength as a constant, $\tau_L/\lambda_p = const.$
3. Scale the laser spot size over the plasma wavelength as a constant, $w_0/\lambda_p = const.$
4. Maintain the laser power over the critical power for self-guiding as a constant, $P/P_c = const.$
5. The plasma density, laser pulse duration, and the laser spot size only scale with laser wavelength (laser frequency), thus for the same P/P_c, a_0 stays the same.

Then we choose one parameter set from the map in Fig. 4(c) where $a_0^{LP} = 1.6$, $n_e = 4.0 \times 10^{18}$ cm^{-3} as references to scale to long wavelength with both CP and LP lasers. For all simulations, the spatial and temporal resolution are fixed as $dz = \lambda_L/32$, $dr = \lambda_L/3$, $dt = T_L/32$, the number of particles per cell is fixed as 16, the number of modes is fixed as 2, the moving window size is fixed as 62.5 λ_L × 150 λ_L in z and r directions, respectively.

As a result, the evolution of the injected electron beam charge as a function of laser wavelength for LP and CP cases are given in Fig. 6(a) and (b), respectively. The correlation of beam charge and laser wavelength is more complex than a linear relationship due to plasma temperature increase[56]. Figure 6(c) summarizes the normalized charge comparison between CP and LP cases for all laser wavelengths. Surprisingly, the relative importance of polarization oscillates between CP and LP, from which we can identify distinct wavelength regimes. As we have discussed above in Sec. III, CP corresponds to a higher normalized beam charge ($Q_{CP}/(Q_{CP}+Q_{LP}) \simeq 70\%$) in the case of 800 nm lasers; and in the case of $\lambda_L \in [8.0 - 10.0]$ μm and $\lambda_L > 17.5$ μm, the normalized beam charge in CP cases reaches approximately 100%. While in the case of $\lambda_L \in [4.5 - 6.0]$ μm and $\lambda_L \in [14.0 - 16.0]$ μm, the normalized beam charge in LP cases also reaches approximately 100%. This might indicate a more complicated injection mechanism rather than the typical self-injection and the "ATI injection" as discussed above.

Before elucidating the injection mechanisms, we first examined the plasma density distribution for several different laser wavelengths, as shown in Fig. 7(a)-(j). As

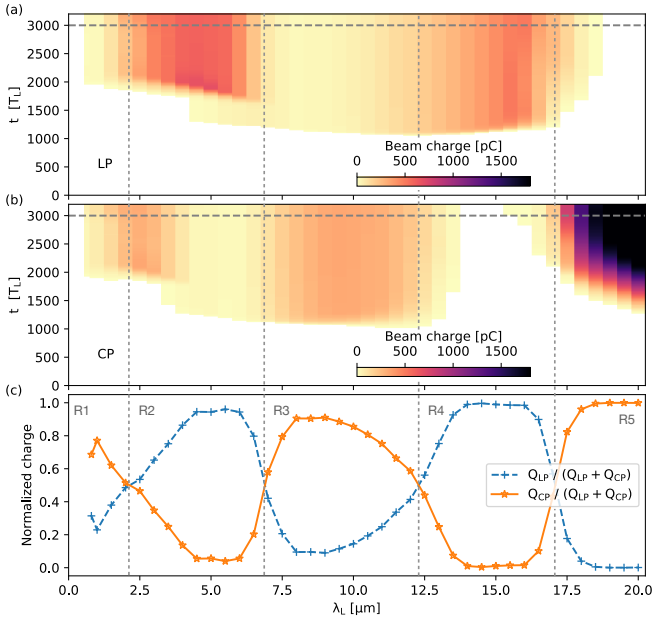

FIG. 6. Evolution of injected electron beam charges as a function of laser wavelength for (a) LP and (b) CP cases, respectively. (c) Normalized charge comparison between CP and LP as a function of laser wavelength. The beam charges for all simulations are extracted at the same time step at $t = 3000\ T_L$. There are five distinct regions where either the charge is larger for CP or LP, which are identified R1-R5.

the laser wavelength increases, the bubble shape changes significantly; the difference between CP and LP cases for the same wavelength becomes more and more pronounced. For the short wavelength case, see Fig. 7(a) with $\lambda_L = 0.8$ μm, the bubble structures are quite similar between CP and LP cases, as we have discussed in Sec. III, although the ionization front for CP falls behind slightly due to a slightly higher ionization threshold on electric field. As we continue to increase the laser wavelength, a double-layered bubble sheath emerges, as in Fig. 7(b) - (f). This also corresponds to a density decrease on the bubble sheath. In addition, the second ionization front falls behind even more for the CP cases compared with the LP cases. For laser wavelength $\lambda_L \gtrsim 12.5$ μm, the bubble structure starts shrinking and is almost invisible for the CP cases. Eventually the bubble structure vanishes for the LP cases as well for $\lambda_L \gtrsim 16.5$ μm. Figure 7(k) and (l) compares the bubble width as a function of laser wavelength for CP and LP cases, respectively. At the short wavelength limit, the bubble sheath has high density spikes and a narrow width. As the laser wavelength increases, the sheath density decreases and the width increases mainly due to the high plasma temperature, especially for the CP cases. Notably the laser wavelength threshold of bubble vanishing for CP is lower than LP. That is mainly due to the different laser intensity evolution so that LP results in a higher laser intensity.

Now, we will elucidate the injection mechanisms for

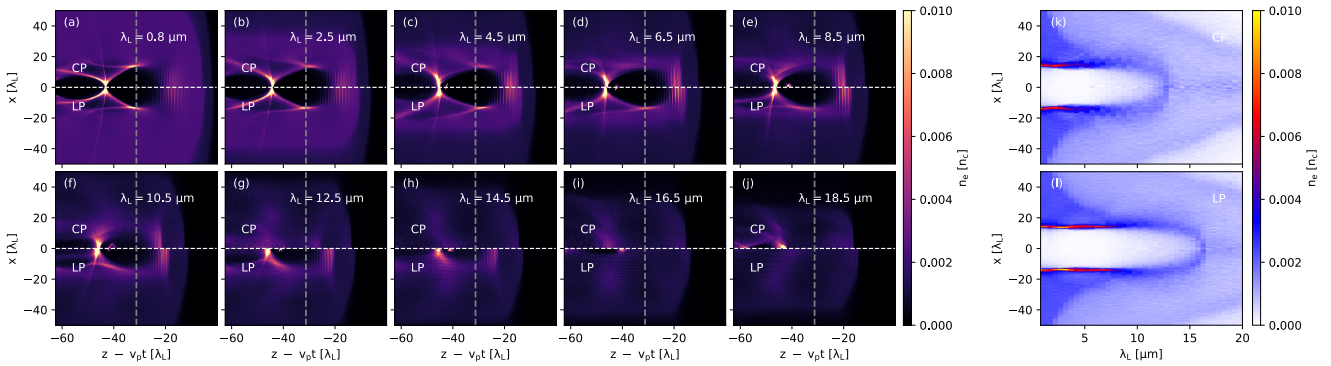

FIG. 7. (a)-(j) Laser wavelength effects on the plasma distribution between CP and LP cases. All snapshots were taken at the same time step at $t = 1500\ T_L$. (k) and (l) show the plasma bubble width as a function of laser wavelength for CP and LP cases, respectively. All lineouts are taken at the same location as indicated by the vertical dashed lines in (a)-(j).

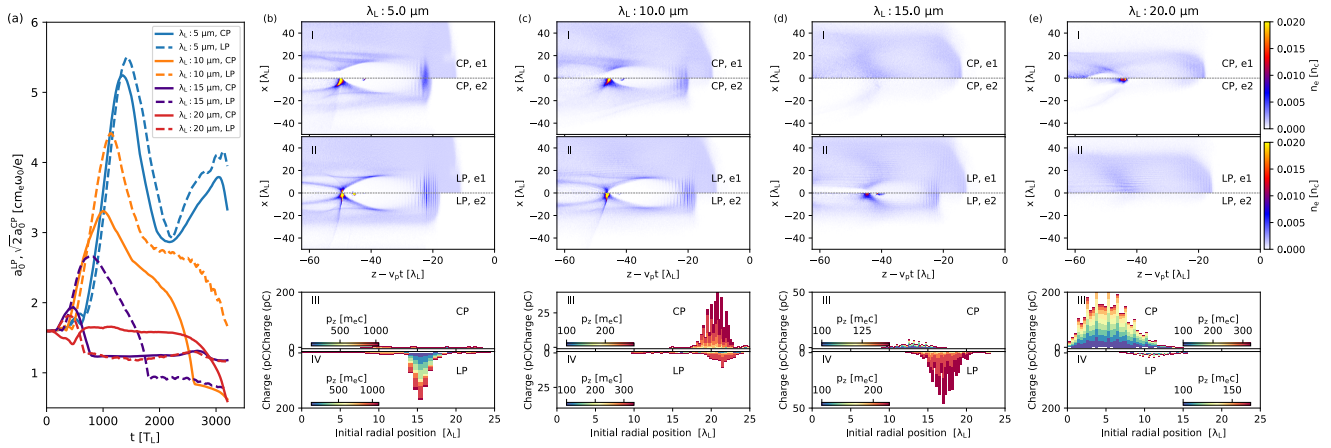

FIG. 8. (a) Evolution of normalized peak laser intensities with 4 different laser wavelength at 5, 10, 15 and 20 μm. The corresponding plasma density distributions and initial radial positions for the injected electrons are given in in (b) - (e). For each of them, (I) and (II) give the density distribution for both e_1 (upper) and e_2 (lower) for the CP and LP cases, respectively. (III) and (IV) show the distribution as the initial radial position of the injected electrons for CP and LP case, respectively.

different wavelength regimes R2-R5 in Fig. 6(c); the first region R1 at short wavelength has been discussed in Sec. III. To characterize these regions, we further investigated the simulations at wavelengths of 5, 10, 15 and 20 μm, which are characteristic of the behavior in the regions R2, R3, R4 and R5 respectively. Figure 8(a) compares the peak laser intensities between CP and LP for those wavelengths. There are several obvious features that can be observed. First, the laser intensity for CP is higher than that in LP, especially when injection starts ($\sim 1300\ T_L$ for all the 4 wavelength), except for the case of $\lambda_L = 20\ \mu$m. Second, the longer the laser wavelength, the lower the peak laser intensity when injection happens. Third, the case of $\lambda_L = 5\ \mu$m displays a second intensity peak.

For the case of $\lambda_L = 5\ \mu$m (region R2) in which LP results in higher electron beam charge, the injection mechanisms for CP and LP cases are different. In fact, there are two injection mechanisms occurring in the LP case, while only one in the CP case. The injection in the CP case and the first injection of the LP case starts around roughly the same time and all the electrons are from $e2$, which indicates that the mechanism for this injection is due to ATI. The second injection in the LP case happens much later than that in the CP case, as can be seen from the comparison of the beam positions in the plasma bubble in Fig. 8(b) (I) and (II), around the starting point of the second laser intensity peak. This peak is mainly due to the self-steepening of the laser pulse due to the ionization front erosion[39,40] and resulting notable carrier-envelope-phase (CEP) effects. Such effects are more pronounced in region R2 than that in region R1. And CEP effects cause the asymmetry of the bubble structure that leads to injection in LP case since the asymmetry is in the plane of the laser polarization[57,58]. CP lasers suffer less from the CEP effects due to the fact that the electric field rotates transversely, thus no injection happens due to CEP effects for CP. Note that the beam charge due

to the ATI process is negligible compared to that of the CEP effects for LP.

For the case of $\lambda_L = 10$ μm (region R3), we observed more injected beam charge in the CP case. In both CP and LP cases, the injected electrons are almost completely from $e2$, which indicates the injection is dominated by the ATI process for both. The situation in the LP case here is slightly different from the LP case of 800 nm, as in that case there is a significant number of electrons from $e1$. The difference is mainly due to the higher temperature effects which will be discussed in detail later in this section.

For the case of $\lambda_L = 15$ μm (region R4), there is no injection observed in the CP case. The injection in the LP case is a result of a combination of ATI injection, thermal injection and the influence of the laser intensity evolution. As one can see from Fig. 8(a), the CP laser intensity drops quickly after the the first peak, while the LP laser intensity maintains relatively high for a much longer time. When injection happens around $t = 1300\ T_L$ in the LP case, the CP laser intensity is already lower than the initial intensity, thus results in no injection. Meanwhile, the injected electrons for LP case are all from $e2$, indicates the injection mechanism as ATI injection and thermal effects.

For the case of $\lambda_L = 20$ μm (region R5), we only observed injection in the CP case, and all the injected electrons resulted from $e2$. As we have discussed above that the electric field strength hence the laser intensity threshold for ATI scales with laser wavelength as $E_L \propto a_0/\lambda_L$. For the same electric field strength, the increase of the laser wavelength corresponds to an increase of the laser intensity. For $\lambda_L = 20$ μm, the required normalized laser intensity to ionize $e2$ is $a_i \simeq 1.6$ (for CP) which is slightly higher than the initial laser intensity. That means in this case, electrons can only be released at the peak of the laser pulse intensity profile. This is the basic scenario for ionization injection[46–48]. As we can see from the plasma distribution in Fig. 8(e)(I), the plasma wave is mainly made of $e1$, while electrons from $e2$ are well confined around the peak location of the laser pulse and the rear of the bubble, indicating ionization injection. In addition, we examined the initial radial positions of the injected electrons, as shown in Fig. 8(e)(III). All the injected electrons are from a much smaller initial radial position, comparing from the cases of other wavelength in Fig. 8(b)-(d). This indicates the fact that they were ionized around the peak of the laser pulse, which is a direct evidence of ionization injection. Ionization injection has a negligible dependence on laser polarization, thus we should be able to observe injection in the LP case as well. However, as shown in Fig. 8(a), the LP laser intensity in this case is lower than that of the CP case, thus no $e2$ electrons can be released. Ionization injection has to the best of our knowledge not been reported as the main injection mechanism with 800 nm lasers with low Z target gases such as hydrogen and helium. That is mainly due to the fact that the ATI threshold intensity can be easily achieved at the laser pulse front for TW level lasers.

We have briefly mentioned plasma temperature effects on injection; here we take the case of $\lambda_L = 10$ μm as an example to elucidate the temperature effects. Thermal effects are known to limit the wave amplitude and affect the trapping condition[29–38], and so as the temperature increases due to ATI, we should expect the trapped charge to be influenced by thermal effects. Figure 9 demonstrates the comparison of four different cases with CP and LP lasers, neutral helium and pre-ionized cold plasma targets. With neutral helium targets, both CP and LP results in beam injection, as shown in Fig. 9(a) and (b), while the total beam charge is higher in the CP case. This is mainly due to the ATI process, as discussed above. However, in the case with pre-ionized cold plasma, no injection is observed with either CP or LP lasers. There is almost no difference in the plasma density distribution, as we can see from Fig. 9(g) and (h). For the cases with LP laser, neutral helium target results in clear injection, see Fig. 9(b), comparing with the pre-ionized plasma case in Fig. 9(d). The comparison of the corresponding transverse plasma density distribution shows clearly the decrease of the bubble sheath density and the increase of bubble sheath thickness, as shown in Fig. 9(f) and (h). This is mainly due to the considerable plasma temperature at long wavelength due to ATI, as shown in Fig. 2. As in the case of CP with neutral he-

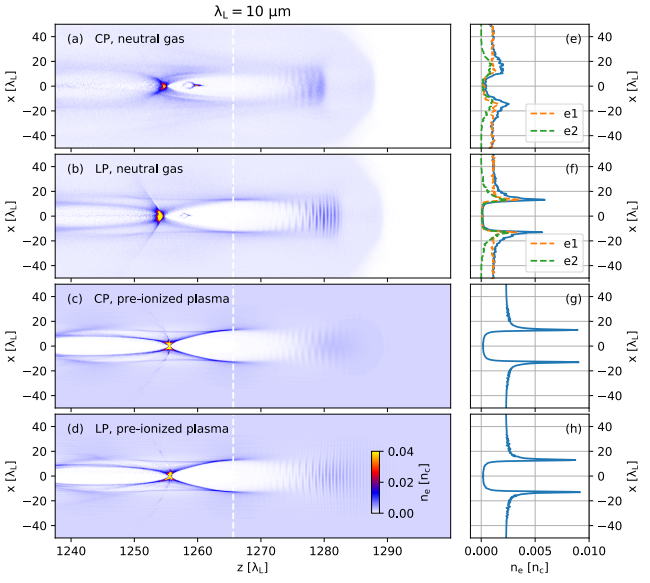

FIG. 9. Comparison of plasma density distributions among 4 difference cases with the same laser wvaelength as $\lambda_L = 10$ μm: (a) with CP laser and neutral gas target, (b) LP laser and neutral gas target, (c) CP laser and pre-ionized plasma and (d) LP laser with pre-ionized plasma. The snapshots are taken at the same time step at $t = 1300\ T_L$. (e) - (f) show the density lineouts corresponding to a longitudinal location indicted by the dashed line for the cases in (a) - (d). In (e) and (f), the density profile contributed by two helium electrons were given separately.

TABLE I. Summary of the mechanisms affecting electron injection for both LP and CP cases in the distinct regions identified in Fig. 6.

Region	LP	CP
R1	Weak ATI assisted injection	ATI assisted injection
R2	Ionization pulse steepening / CEP oscillation & ATI assisted injection	Ionization pulse steepening / Reduced ATI assisted injection
R3	ATI assisted injection & strong thermal effects	ATI assisted injection & strong thermal effects
R4	ATI assisted injection & strong thermal effects	Injection suppressed as wake amplitude diminished
R5	Injection suppressed as wake amplitude diminished	Ionization injection

lium, due to the extremely hot temperature, ∼100 keV, the density spike almost completely disappeared, as we can see from Fig. 9(e). Thus, the comparison between the cases of neutral helium and pre-ionized cold plasma with long laser wavelength, as well as the comparison between cases of short and long laser wavelength with neutral helium targets illustrates the modification of the injection mechanism by thermal effects.

Table I summarizes these main physical processes contributing to electron injection mechanisms in the regimes identified in Fig. 6.

V. CONCLUSIONS

In conclusion, we have investigated the role of laser polarization and wavelength on the electron injection mechanisms in LWFA. The laser polarization effects are primarily due to the ATI process. We revealed a distinctive injection mechanism with CP laser due to the non-vanishing phase-dependent vector potential and higher momentum and kinetic energy gain due to ATI, compared with the case of a LP laser. Such a mechanism was confirmed by experimental observations that CP laser enhanced the injected beam charge and lowered the injection threshold at a laser wavelength of 800 nm, together with the evidence of a higher plasma temperature with XUV measurements.

As the laser wavelength increases, wavelength effects on electron injection emerge due to the strong correlation between ATI processes and the laser wavelength. The laser wavelength also affects the laser pulse evolution in plasma and the plasma temperature, which also play significant roles in electron injection. In the laser wavelength range of 0.8 - 20 μm, we discovered an interesting phenomenon that the injected beam charge comparison between LP and CP cases perform periodic oscillations where LP and CP both dominate certain wavelength ranges. Such oscillations highlight the interplay between several different injection regimes, including ATI injection, injection by CEP effects, ionization injection and thermal effects.

Therefore, our study sheds light on the understanding of the complexity of electron injection dynamics in a laser wakefield accelerator by illustrating several different injection mechanisms due to the laser polarization and wavelength effects. This could be crucial for generating high quality and highly controllable electron beams for various applications. Tuning both the driving wavelength and the polarization of the laser may enable precise control of the generated electron beam properties.

ACKNOWLEDGEMENTS

This material is based upon work supported by the National Science Foundation under Grant No. PHY-1753165. This work was supported by DOE Office of Science, Fusion Energy Sciences under Award No. DE-SC0019255: the LaserNetUS initiative at the Gérard Mourou Center for Ultrafast Optical Sciences and Grant No. DE- SC0019186 and the AFOSR Grant No. FA9550-19-1-0072. The experiments were conducted at the HERCULES facility developed with support from the National Science Foundation under award MRI Grant No. 1725482. The work of D. S. was supported by AFOSR Grant No. FA9550-16-1-0121. The work of S. H. was supported by U.S. Department of Energy, Office of Science Early Career Research Program, Office of Fusion Energy Sciences under Award No. FWP-14-017426 and Sandia National Laboratories. Sandia National Laboratories is a multimission laboratory managed and operated by National Technology & Engineering Solutions of Sandia, LLC, a wholly owned subsidiary of Honeywell International Inc., for the U.S. Department of Energy's National Nuclear Security Administration under contract DE-NA0003525. This paper describes objective technical results and analysis. Any subjective views or opinions that might be expressed in the paper do not necessarily represent the views of the U.S. Department of Energy or the United States Government. The development of EPOCH was in part funded by the UK EPSRC Grants No. EP/G054950/1, No. EP/G056803/1, No. EP/ G055165/1, and No. EP/M022463/1. This research was supported in part through computational resources and services provided by Advanced Research Computing at the University of Michigan, Ann Arbor.

DATA AVAILABILITY

The data that support the findings of this study are available from the corresponding author upon reasonable request.

[1] T. Tajima and J. M. Dawson, Phys. Rev. Lett. **43**, 267 (1979).
[2] E. Esarey, C. B. Schroeder, and W. P. Leemans, Rev. Mod. Phys. **81**, 1229 (2009).
[3] S. P. D. Mangles, C. D. Murphy, Z. Najmudin, A. G. R. Thomas, J. L. Collier, A. E. Dangor, E. J. Divall, P. S. Foster, J. G. Gallacher, C. J. Hooker, D. A. Jaroszynski, A. J. Langley, W. B. Mori, P. A. Norreys, F. S. Tsung, R. Viskup, B. R. Walton, and K. Krushelnick, Nature **431**, 535 (2004).
[4] C. G. R. Geddes, C. Toth, J. van Tilborg, E. Esarey, C. B. Schroeder, D. Bruhwiler, C. Nieter, J. Cary, and W. P. Leemans, Nature **431**, 538 (2004).
[5] J. Faure, Y. Glinec, A. Pukhov, S. Kiselev, S. Gordienko, E. Lefebvre, J. P. Rousseau, F. Burgy, and V. Malka, Nature **431**, 541 (2004).
[6] A. J. Gonsalves, K. Nakamura, J. Daniels, C. Benedetti, C. Pieronek, T. C. H. de Raadt, S. Steinke, J. H. Bin, S. S. Bulanov, J. van Tilborg, C. G. R. Geddes, C. B. Schroeder, C. Tóth, E. Esarey, K. Swanson, L. Fan-Chiang, G. Bagdasarov, N. Bobrova, V. Gasilov, G. Korn, P. Sasorov, and W. P. Leemans, Phys. Rev. Lett. **122**, 084801 (2019).
[7] W. P. Leemans, A. J. Gonsalves, H.-S. Mao, K. Nakamura, C. Benedetti, C. B. Schroeder, C. Tóth, J. Daniels, D. E. Mittelberger, S. S. Bulanov, J.-L. Vay, C. G. R. Geddes, and E. Esarey, Phys. Rev. Lett. **113**, 245002 (2014).
[8] H. T. Kim, K. H. Pae, H. J. Cha, I. J. Kim, T. J. Yu, J. H. Sung, S. K. Lee, T. M. Jeong, and J. Lee, Phys. Rev. Lett. **111**, 165002 (2013).
[9] X. Wang, R. Zgadzaj, N. Fazel, Z. Li, S. A. Yi, X. Zhang, W. Henderson, Y. Y. Chang, R. Korzekwa, H. E. Tsai, C. H. Pai, H. Quevedo, G. Dyer, E. Gaul, M. Martinez, A. C. Bernstein, T. Borger, M. Spinks, M. Donovan, V. Khudik, G. Shvets, T. Ditmire, and M. C. Downer, Nature Communications **4**, 1988 (2013).
[10] F. Albert, M. E. Couprie, A. Debus, M. C. Downer, J. Faure, A. Flacco, L. A. Gizzi, T. Grismayer, A. Huebl, C. Joshi, M. Labat, W. P. Leemans, A. R. Maier, S. P. D. Mangles, P. Mason, F. Mathieu, P. Muggli, M. Nishiuchi, J. Osterhoff, P. P. Rajeev, U. Schramm, J. Schreiber, A. G. R. Thomas, J.-L. Vay, M. Vranic, and K. Zeil, New Journal of Physics **23**, 031101 (2021).
[11] W. Leemans and E. Esarey, Physics Today **62**, 44 (2009), https://doi.org/10.1063/1.3099645.
[12] A. Debus, R. Pausch, A. Huebl, K. Steiniger, R. Widera, T. E. Cowan, U. Schramm, and M. Bussmann, Phys. Rev. X **9**, 031044 (2019).
[13] J. P. Palastro, J. L. Shaw, P. Franke, D. Ramsey, T. T. Simpson, and D. H. Froula, Phys. Rev. Lett. **124**, 134802 (2020).
[14] C. Caizergues, S. Smartsev, V. Malka, and C. Thaury, Nature Photonics **14**, 475 (2020).
[15] A. R. Maier, N. M. Delbos, T. Eichner, L. Hübner, S. Jalas, L. Jeppe, S. W. Jolly, M. Kirchen, V. Leroux, P. Messner, M. Schnepp, M. Trunk, P. A. Walker, C. Werle, and P. Winkler, Phys. Rev. X **10**, 031039 (2020).
[16] F. Grüner, S. Becker, U. Schramm, T. Eichner, M. Fuchs, R. Weingartner, D. Habs, J. Meyer-ter Vehn, M. Geissler, M. Ferrario, L. Serafini, B. van der Geer, H. Backe, W. Lauth, and S. Reiche, Applied Physics B **86**, 431 (2007).
[17] A. Bernhard, V. A. Rodríguez, S. Kuschel, M. Leier, P. Peiffer, A. Sävert, M. Schwab, W. Werner, C. Widmann, A. Will, A.-S. Müller, and M. Kaluza, Nuclear Instruments and Methods in Physics Research Section A: Accelerators, Spectrometers, Detectors and Associated Equipment **909**, 391 (2018), 3rd European Advanced Accelerator Concepts workshop (EAAC2017).
[18] J. M. Cole, K. T. Behm, E. Gerstmayr, T. G. Blackburn, J. C. Wood, C. D. Baird, M. J. Duff, C. Harvey, A. Ilderton, A. S. Joglekar, K. Krushelnick, S. Kuschel, M. Marklund, P. McKenna, C. D. Murphy, K. Poder, C. P. Ridgers, G. M. Samarin, G. Sarri, D. R. Symes, A. G. R. Thomas, J. Warwick, M. Zepf, Z. Najmudin, and S. P. D. Mangles, Phys. Rev. X **8**, 011020 (2018).
[19] K. Poder, M. Tamburini, G. Sarri, A. Di Piazza, S. Kuschel, C. D. Baird, K. Behm, S. Bohlen, J. M. Cole, D. J. Corvan, M. Duff, E. Gerstmayr, C. H. Keitel, K. Krushelnick, S. P. D. Mangles, P. McKenna, C. D. Murphy, Z. Najmudin, C. P. Ridgers, G. M. Samarin, D. R. Symes, A. G. R. Thomas, J. Warwick, and M. Zepf, Phys. Rev. X **8**, 031004 (2018).
[20] C. N. Danson, C. Haefner, J. Bromage, T. Butcher, J.-C. F. Chanteloup, E. A. Chowdhury, A. Galvanauskas, L. A. Gizzi, J. Hein, D. I. Hillier, and et al., High Power Laser Science and Engineering **7**, e54 (2019).
[21] A. Pukhov and J. Meyer-ter Vehn, Applied Physics B **74**, 355 (2002).
[22] W. Lu, M. Tzoufras, C. Joshi, F. S. Tsung, W. B. Mori, J. Vieira, R. A. Fonseca, and L. O. Silva, Phys. Rev. ST Accel. Beams **10**, 061301 (2007).
[23] Y. Ma, L. M. Chen, N. A. M. Hafz, D. Z. Li, K. Huang, W. C. Yan, J. Dunn, Z. M. Sheng, and J. Zhang, Applied Physics Letters **105**, 161110 (2014), https://doi.org/10.1063/1.4900412.
[24] S. Corde, C. Thaury, A. Lifschitz, G. Lambert, K. Ta Phuoc, X. Davoine, R. Lehe, D. Douillet, A. Rousse, and V. Malka, Nature Communications **4**, 1501 (2013).
[25] P. B. Corkum, N. H. Burnett, and F. Brunel, Phys. Rev. Lett. **62**, 1259 (1989).
[26] C. I. Moore, A. Ting, S. J. McNaught, J. Qiu, H. R. Burris, and P. Sprangle, Phys. Rev. Lett. **82**, 1688 (1999).
[27] C. I. Moore, A. Ting, T. Jones, E. Briscoe, B. Hafizi, R. F. Hubbard, and P. Sprangle, Physics of Plasmas **8**, 2481 (2001).
[28] B. Zhou, A. Houard, Y. Liu, B. Prade, A. Mysyrowicz, A. Couairon, P. Mora, C. Smeenk, L. Arissian, and P. Corkum, Phys. Rev. Lett. **106**, 255002 (2011).
[29] T. Katsouleas and W. B. Mori, Phys. Rev. Lett. **61**, 90 (1988).
[30] J. B. Rosenzweig, Phys. Rev. A **38**, 3634 (1988).
[31] Z. M. Sheng and J. Meyer-ter Vehn, Physics of Plasmas **4**, 493 (1997), https://doi.org/10.1063/1.872116.
[32] C. B. Schroeder, E. Esarey, and B. A. Shadwick, Phys. Rev. E **72**, 055401 (2005).
[33] R. M. G. M. Trines and P. A. Norreys, Physics of Plasmas **13**, 123102 (2006), http://dx.doi.org/10.1063/1.2398927.
[34] E. Esarey, C. B. Schroeder, E. Cormier-Michel, B. A. Shadwick, C. G. R. Geddes, and W. P. Leemans, Physics of Plasmas **14**, 056707 (2007), http://dx.doi.org/10.1063/1.2714022.
[35] T. Coffey, Physics of Plasmas **17**, 052303 (2010), http://dx.doi.org/10.1063/1.3418351.
[36] D. A. Burton and A. Noble, Journal of Physics A: Mathematical and Theoretical **43**, 075502 (2010).
[37] S. V. Bulanov, T. Z. Esirkepov, M. Kando, J. K. Koga, A. S. Pirozhkov, T. Nakamura, S. S. Bulanov, C. B. Schroeder, E. Esarey, F. Califano, and F. Pegoraro, Physics of Plasmas **19**, 113102 (2012), http://dx.doi.org/10.1063/1.4764052.
[38] A. G. R. Thomas, Phys. Rev. E **94**, 053204 (2016).
[39] Z.-H. He, J. A. Nees, B. Hou, K. Krushelnick, and A. G. R. Thomas, Phys. Rev. Lett. **113**, 263904 (2014).
[40] Z.-H. He, J. A. Nees, B. Hou, K. Krushelnick, and A. G. R. Thomas, Plasma Physics and Controlled Fusion **56**, 084010 (2014).
[41] Y. Ma, D. Seipt, A. E. Hussein, S. Hakimi, N. F. Beier, S. B. Hansen, J. Hinojosa, A. Maksimchuk, J. Nees, K. Krushelnick, A. G. R. Thomas, and F. Dollar, Phys. Rev. Lett. **124**, 114801 (2020).
[42] T. D. Arber, K. Bennett, C. S. Brady, A. Lawrence-Douglas, M. G. Ramsay, N. J. Sircombe, P. Gillies, R. G. Evans, H. Schmitz, A. R. Bell, and C. P. Ridgers, Plasma Physics and Controlled Fusion **57**, 1 (2015).

[43]M. V. Ammosov, N. B. Delone, and V. P. Krainov, Sov. Phys. JETP **64**, 1191 (1986).
[44]S. Augst, D. Strickland, D. D. Meyerhofer, S. L. Chin, and J. H. Eberly, Phys. Rev. Lett. **63**, 2212 (1989).
[45]R. Lehe, M. Kirchen, I. A. Andriyash, B. B. Godfrey, and J.-L. Vay, Computer Physics Communications **203**, 66 (2016).
[46]M. Chen, Z. M. Sheng, Y. Y. Ma, and J. Zhang, Journal of Applied Physics **99**, 1 (2006).
[47]C. McGuffey, A. G. R. Thomas, W. Schumaker, T. Matsuoka, V. Chvykov, F. J. Dollar, G. Kalintchenko, V. Yanovsky, A. Maksimchuk, K. Krushelnick, V. Y. Bychenkov, I. V. Glazyrin, and A. V. Karpeev, Phys. Rev. Lett. **104**, 025004 (2010).
[48]A. Pak, K. A. Marsh, S. F. Martins, W. Lu, W. B. Mori, and C. Joshi, Phys. Rev. Lett. **104**, 025003 (2010).
[49]P. Sprangle, C. Tang, and E. Esarey, IEEE Transactions on Plasma Science **15**, 145 (1987).
[50]M. Vargas, W. Schumaker, Z.-H. He, Z. Zhao, K. Behm, V. Chvykov, B. Hou, K. Krushelnick, A. Maksimchuk, V. Yanovsky, and A. G. R. Thomas, Applied Physics Letters **104**, 174103 (2014).
[51]S. Kuschel, M. B. Schwab, M. Yeung, D. Hollatz, A. Seidel, W. Ziegler, A. Sävert, M. C. Kaluza, and M. Zepf, Phys. Rev. Lett. **121**, 154801 (2018).
[52]B. M. Penetrante and J. N. Bardsley, Phys. Rev. A **43**, 3100 (1991).
[53]N. Lemos, T. Grismayer, L. Cardoso, J. Geada, G. Figueira, and J. M. Dias, Phys. Plasmas **20**, 103109 (2013).
[54]S. Hansen, J. Bauche, C. Bauche-Arnoult, and M. Gu, High Energy Density Physics **3**, 109 (2007).
[55]D. Neely, D. Chambers, C. Danson, P. Norreys, S. Preston, F. Quinn, M. Roper, J. Wark, and M. Zepf, in *Superstrong Fields in Plasmas*, AIP Conf. Proc. No. 426, edited by M. Lontano, G. Mourou, F. Pegoraro, and E. Sindoni (AIP, New York, 1998) pp. 479–484.
[56]E. Esarey, C. B. Schroeder, E. Cormier-Michel, B. A. Shadwick, C. G. R. Geddes, and W. P. Leemans, Physics of Plasmas **14**, 056707 (2007).
[57]Y. Ma, L. Chen, D. Li, W. Yan, K. Huang, M. Chen, Z. Sheng, K. Nakajima, T. Tajima, and J. Zhang, Scientific Reports **6**, 30491 (2016).
[58]E. N. Nerush and I. Y. Kostyukov, Phys. Rev. Lett. **103**, 035001 (2009).